Climate of the Past

Open Access

Dating a tropical ice core by time–frequency analysis of ion concentration depth profiles

M. Gay[1], M. De Angelis[2], and J.-L. Lacoume[1]

[1]GIPSA-lab, 11 rue des mathématiques, 38402 Saint-Martin-d'Hères, France
[2]CNRS/Université Joseph Fourier, LGGE, 54 rue Molière, 38402 Saint-Martin-d'Hères, France

Correspondence to: M. Gay (michel.gay@gipsa-lab.grenoble-inp.fr)

Abstract. Ice core dating is a key parameter for the interpretation of the ice archives. However, the relationship between ice depth and ice age generally cannot be easily established and requires the combination of numerous investigations and/or modelling efforts. This paper presents a new approach to ice core dating based on time–frequency analysis of chemical profiles at a site where seasonal patterns may be significantly distorted by sporadic events of regional importance, specifically at the summit area of Nevado Illimani (6350 m a.s.l.), located in the eastern Bolivian Andes (16°37′ S, 67°46′ W). We used ion concentration depth profiles collected along a 100 m deep ice core. The results of Fourier time–frequency and wavelet transforms were first compared. Both methods were applied to a nitrate concentration depth profile. The resulting chronologies were checked by comparison with the multi-proxy year-by-year dating published by de Angelis et al. (2003) and with volcanic tie points. With this first experiment, we demonstrated the efficiency of Fourier time–frequency analysis when tracking the nitrate natural variability. In addition, we were able to show spectrum aliasing due to under-sampling below 70 m. In this article, we propose a method of de-aliasing which significantly improves the core dating in comparison with annual layer manual counting. Fourier time–frequency analysis was applied to concentration depth profiles of seven other ions, providing information on the suitability of each of them for the dating of tropical Andean ice cores.

1 Introduction

Ice core dating, i.e. establishing a univocal relationship between ice depth and age, is not easy, yet is fundamental for the interpretation of ice archives. Current methods generally combine various approaches such as identifying annual snow layers by seasonal features in high-resolution records, location of specific physico-chemical patterns previously identified in well-dated sedimentary or ice archives, and an inverse approach.

Annual layer counting is well suited to the study of high-frequency atmospheric processes, but requires a certain amount of refinement, due to uncertainty in identifying individual layers. In particular, the annual signal may be distorted or smoothed by changes in the snow accumulation rate and processes involved in snow deposition and firn aging: snow blowing, wind pumping, water vapour or gradient diffusion, and interaction between reactive species may significantly modify the initial registers. Dating uncertainty increases with depth, making it very useful to identify any paleo-events which allow the synchronization of different ice cores and potentially to check the current dating (Narcisi et al., 2005; Traufetter et al., 2004).

The large number of studies undertaken over polar ice caps since the end of the 1950s has helped to improve considerably our understanding of processes leading to the building of polar ice records and their dating for at least the central areas of Antarctica and Greenland. The comparison between deep ice cores recovered in central Greenland and in Antarctica as well as marine sediment cores has provided even more accurate ice chronologies for time periods covering the most recent decades or the past few centuries as well as several

hundred kyr (Ruth et al., 2007; Lemieux et al., 2010). A typical example is the multi-parameter approach combining the identification of seasonal maxima along chemical profiles and age matching with specific climatic and volcanic events used as tie points, which provided a year-by-year dating of the GISP2 ice core for the past 100 kyr (Meese et al., 1997). In addition to model timescales, a new Greenland timescale has been more recently developed back to 60 kyr before AD 2000, based on the identification of annual layers along a large set of high-resolution records of ice chemical and physical properties (Andersen et al., 2006; Svensson et al., 2005, 2008; Rasmussen et al., 2008). The thorough comparison of annual layer counting carried out by independent experienced investigators greatly improved the dating accuracy, but is a tedious, time-consuming effort that highlights the need for automated and less subjective methods.

The study of Andean ice records started in the mid-1980s with paleo-climate reconstructions based on the comparison of water stable isotope profiles with Antarctic or Greenland data (Thompson et al., 1998, 2003). More recently, studies have focused specifically on understanding the atmospheric natural variability on the annual and inter-annual timescales (de Angelis et al., 2003; Correia et al., 2003; Schotterer et al., 2003; Vimeux et al., 2008). However, logistical constraints and harsh weather conditions prevailing over the high-altitude cold glaciers of the Andean Cordillera often make it difficult to obtain the full set of glaciological and meteorological data required by the exploitation of Andean ice archives. Thus, improving the dating of the cores by developing reliable dating tools remains a key challenge. Particular attention must be paid to sublimation processes and snow remobilization by wind, which is suspected of playing a prominent role at sites influenced by major cyclonic activity or seasonal convection. Moreover, the rich and intricate fingerprint of Andean volcanism superimposes the long-range influence of cataclysmic eruptions commonly used as time markers for polar ice cores. Nevertheless, most Andean ice cores were recovered in the tropical belt, where the precipitation system is characterized by the yearly alternation of a warm season (around NDJ) and a colder dry season (around JJA) accompanied by significant changes in agricultural practices, soil emissions, and air mass trajectories. Biomass burning, increased aridity, and soil dust mobilization send large amounts of aerosol and gases into the tropical atmosphere, mostly during the dry season at the same time as limited water vapour condensation and/or riming, which occur at the surface of falling snow crystals. As a consequence, the concentration of chemical species in fresh snow should be significantly higher during the dry season than during the wet season. Regarding non-volatile/non-reactive species in aging surface snow, this seasonal pattern should be enhanced by dry deposition or snow sublimation, which is likely to be more pronounced during the dry season. On this basis, concentration seasonal variability appeared to be a potential dating tool. On the other hand, seasonal trends in ice cores extracted from high-altitude tropical or mid-latitude sites may be partly masked by other components related to the inter-annual variability of source properties (location, emission intensity), synoptic meteorological patterns, or precipitation occurrence. Thus, the identification of the annual layer, independent of the feeling of the observer and attempting to minimize the risk of cumulative errors, appeared to be a useful step.

Various attempts aiming to establish a chronology along sediment or ice cores and based on spectral and wavelet analysis have been developed. Smith et al. (2009) present an automated trace element laminae peak counting procedure based on spectral and wavelet analysis and providing reliable and accurate dating of speleothems with rather regular growth rates. Wheatley et al. (2012) developed a dating method using the autocorrelation function for large-core subsections taken at different depths and reconstructed missing values or unclear annual signals, assuming continuous annual layer thickness. An annual layer detection routine based on the framework of hidden Markov models has been applied by Winstrup et al. (2012) to a stable water isotope record and visual stratigraphy of two Greenland cores showing mainly well-preserved annual signals at great depth and where manual counting has already been carried out. Once all parameters included in the layer model have been optimally chosen by the algorithm according with the layer signal in the data (assumed to be well constrained), the algorithm reproduces the manually counted timescales quite well.

All these studies focus on archives containing well-marked time-related sequences. In particular, automated approaches for annual layer counting along ice cores have almost exclusively been applied to records showing strong and well-constrained seasonal variability, and extracted at sites fully investigated like the Antarctic Peninsula or central Greenland. The context of Andean ice cores is quite different: dating tools remain very limited, and their accuracy is difficult to check.

This paper presents a new approach to ice core dating based on the time–frequency analysis of chemical depth profiles. The method was applied to the upper 100 m (76 m we) of a 137 m deep ice core recovered in 1999 close to the summit of Nevado Illimani in the eastern Bolivian Andes (6350 m a.s.l., 16°37′ S, 67°46′ W). The Illimani ice core was chosen to check the validity of our approach, because (1) continuous high-resolution profiles of 13 inorganic ions and 3 carboxylic ions including valuable markers of the main atmospheric reservoirs on a regional scale were available from the surface to 100 m in depth, (2) preliminary studies of snow accumulation, freshly fallen snow, and the evolution in the composition of surface snow during the dry season were carried out in 2001 and 2002, leading to the expectation of a rather clear seasonal pattern and good preservation of chemical signals in accumulating snow, and (3) year-by-year dating based on annual layer counting was available for the upper part of the core, from the surface to 49.6 m in depth, i.e. from AD 1998 back to AD 1918 (de Angelis et al., 2003).
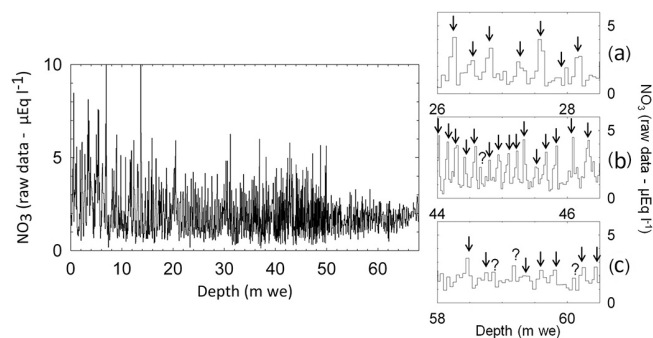
Figure 1. Raw data of $c_{NO_3^-}(d)$ showing the concentration from 0 to 70 m we depth. Arrows denote winter maxima. **(a)** Multi-proxy dating approach (de Angelis et al., 2003); **(b)** and **(c)**: visual counting (this study).

This dating made it necessary to combine the seasonal signals of three wind-borne dust markers (calcium, this study, the mass of insoluble particles, and aluminium, Correia et al., 2003) and two nitrogen ionic species (nitrate and ammonium). Two pure sulfuric acid peaks were observed at 9.13 m and 33.43 m. They were attributed to the stratospheric fallout in early 1993 and 1964, respectively, of the Pinatubo (June 1991) and Mount Agung (March 1963) eruptions. Debris corresponding to the arrival of tropospheric plumes during the 1991 and 1963 dry seasons were found at 10.8 and 33.4–33.8 m, respectively, and used as check points. Dating uncertainty was estimated to be in the range of ±1 yr down to 41 m (AD 1947), and ±2 yr at the bottom of the core section (AD 1919).

Data were processed in two ways. The time–depth relationship was deduced from the time–frequency analysis of the nitrate profile based on Fourier spectrograms, and implemented to construct the ice chronology. A similar approach was then taken using wavelet transforms. In the first part of this article, we first present the raw data and the method we used to compensate for signal bias induced by the experimental sampling rate, which was too low below 68 m, and then we propose and discuss a preliminary dating. The chronologies resulting from the two spectral methods are compared with the chronology proposed for the upper part of the core by de Angelis et al. (2003) and the volcanic tie points defined by these authors. This provides an assessment of the reliability of the two spectral approaches. In the second part, Fourier conjugate transform is applied to the concentration depth profiles of seven other ions, providing seven other independent ice chronologies. The comparison of these 8 independent dating results with each other and with the tie points used by de Angelis et al. (2003) is discussed in terms of method and data suitability.

2 Raw data

In a first step, the method is described and applied to the nitrate concentration depth profile along the Illimani core, $c_{NO_3^-}(d)$. Nitrate is one of the major ions detected in the core, and is less sensitive to post-deposition effects than other biomass markers like formate. Moreover, it is expected to have a strong annual component and not to be markedly affected by sporadic events like volcanic eruptions or dust storms, which can disrupt the seasonal pattern of other ions; therefore it was considered as most suitable for checking our method. Raw data of $c_{NO_3^-}(d)$ are presented in Fig. 1. To counterbalance firn densification, all depths and layer thicknesses will be expressed in metres of water equivalent (m we) in the following sections.

In the left part of Fig. 1, we have reported nitrate concentrations as a function of depth along the whole ice sequence. The three panels in the right part of the figure correspond to selected zoomed sections at 26–28.5 m we (a), 44–46.5 m we (b), and 58–60.5 m we (c), from top to bottom, respectively. The nitrate depth profile clearly shows an alternation of relative maxima denoted by arrows (dry seasons) and minima (wet seasons) corresponding to its annual cycle. Annual layer thickness clearly decreases with depth down to 46 m we (Fig. 1a, b) and then increases again, at the same time as the peak amplitude decreases (Fig. 1c). This trend reversal is discussed in Sect. 4.2.5 in relation to sampling resolution.

3 Method

3.1 Principle

As stated above, our investigation is based on the hypothesis that concentrations of chemical species entrapped in falling snow are periodic in time, with a period of 1 yr. We assume that the variability of the chemical composition of tropical Andean precipitation is controlled by strong seasonal changes in atmospheric properties with a time period of 1 yr. However, and in spite of a good preservation of aging snow, the time dependency of chemical signals cannot be directly inferred from concentration depth profiles, due to the interannual variability of the annual net accumulation rate and to ice thinning through firn densification and ice flow: the annual layer thickness, $a(d)$, varies with depth. A relationship can be written between $a(d)$ and the spatial frequency $f_s(d)$:

$$f_s(d) = \frac{1}{a(d)} \tag{1}$$

The evolution of the spatial frequency associated with the variable periodicity as a function of depth is determined using Fourier time–frequency analysis (Flandrin, 1993; Cohen, 1994) and orthogonal Morlet wavelet transforms (Goupillaud
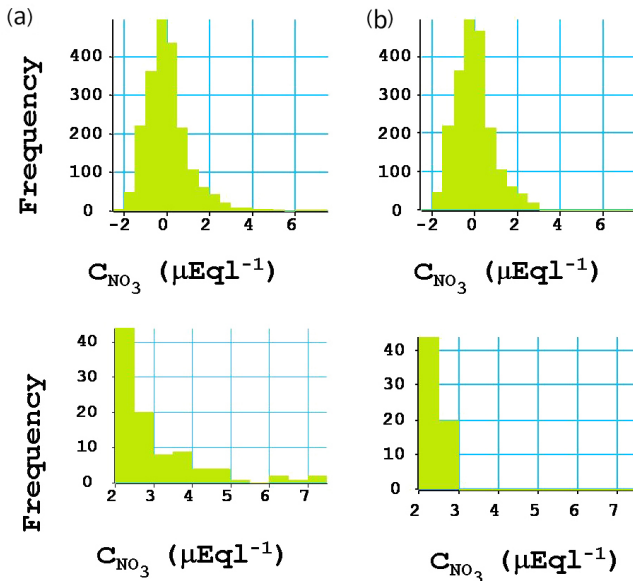
Figure 2. Panel (**a**) top: histogram of raw NO$_3$ concentration; bottom: zoom for the highest concentration values. Panel (**b**) top: histogram of the raw NO$_3$ concentration thresholded; bottom: zoom for the highest concentration values. All histograms have bars of equal width, which is $0.5 \, \mu Eq l^{-1}$.

et al., 1985) applied to the nitrate concentration depth profile. The spatial frequency $f_s(d)$ establishes the relationship linking depth and age, $t(d)$, where $t(d)$ is the age of the layer located at depth d, with the drilling date as the reference time.

In this way, we obtain the time–depth relationship along the part of the Illimani ice core where continuous ion concentration profiles are available, i.e. from the surface to $76.4 \, \text{m}$ we in depth. A comparison is made between results derived from the Fourier time–frequency analysis, the wavelet transforms and a previously published year-by-year dating approach, to evaluate the accuracy of spectral analysis methods applied to chemical species. Independent chronologies are then established using nitrate, formate, oxalate (indicators related to continental biomass), calcium, magnesium, potassium, and sodium (erodible soils) and sulfate (more influenced by volcanism).

3.2 Determination of the age–depth relationship

Let $a(d)$ be the layer thickness corresponding to the depth increase, during a period of one year at depth d. To this spatial period, we relate the spatial frequency

$$f_s(d) = \frac{1}{a(d)} = \frac{dt(d)}{dd}. \tag{2}$$

Let $d_{\min}$ be the depth origin of the determination of the spatial frequency and $t(d)$ the age of the layer/ice at depth d.

The age of the layer at depth d,

$$t(d) = \int_{d_{\min}}^{d} f_s(u) du + t(d_{\min}), \tag{3}$$

gives the relationship between age and depth from the spatial frequency. This relationship is the central point of our method: it shows that the age–depth relationship can be determined from the measurement of the spatial frequency as a function of depth.

4 Data processing

As stated above, data processing is first applied to the nitrate concentration depth profile.

4.1 Data pre-processing

We have a set of 1697 samples of $c_{NO_3^-}(d)$. The nitrate concentration function $c_{NO_3^-}(d)$ is given for a set of depths d not regularly distributed from 0 to $76.4 \, \text{m}$ we. This concentration depth profile has high-amplitude spikes related to particularly intense biomass burning events during the dry season.

Time–frequency analysis requires samples regularly distributed with depth, without high impulses and with a mean value equal to zero. Four interpolation methods were applied to the original data in order to get a concentration profile suitable for spectral analysis: linear, nearest neighbour, Hermite polynomial, and spline.

A thresholding was applied before interpolation, in order to avoid divergence phenomena. We determined the threshold from the histogram of the concentration. The whole histogram of raw concentrations is presented in the upper panel of Fig. 2a, and is zoomed in the lower panel for concentrations higher than $2 \, \mu Eq l^{-1}$. A marked tail in concentration frequency may be observed at $3 \, \mu Eq l^{-1}$, with frequencies remaining very low for concentrations higher than this value. For this reason, concentrations above $3 \, \mu Eq l^{-1}$ were considered to be outliers and were not taken into account. The threshold was thus fixed to $3.25 \, \mu Eq l^{-1}$, a value corresponding to a 0.98 level in the cumulative distribution function[1]. The whole histogram of thresholded concentrations is presented in the upper panel of Fig. 2b, and is zoomed in the lower panel.

A detailed comparison between spatial frequency depth profiles and chronologies obtained using each of the four interpolation methods is presented in the Supplement. This comparison led us to use the spline interpolation in the remaining part of the paper. The nitrate concentration $c_{NO_3^-}(d)$

---

[1]In order to check the value of the threshold, we have compared the qualities (from the criteria given in Eq. (13) and from comparison with the de Angelis et al. (2003) dating) of the dating obtained with a level in the cumulative distribution function varying from 0.99 to 0.95. The best result is obtained with a level of 0.98.
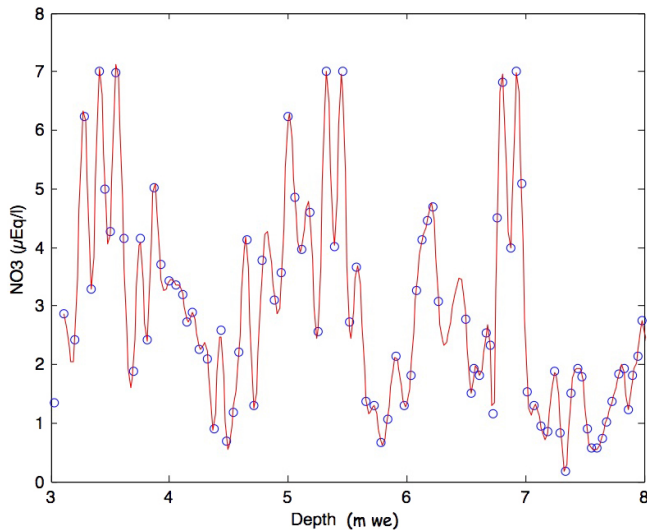
Figure 3. $c_{\mathrm{NO_3^-}}(d)$ raw signal (circles) and the spline interpolation (red line).

Figure 4. Normalized spectra as a function of the spatial frequency of the $\mathrm{NO_3^-}$ concentration depth profile after resampling (spline, 2048 samples) and thresholding. Black line: non-filtered. Green line: filtered by high-pass filtering (cut-off frequency $= 0.5\,(\mathrm{m\,we})^{-1}$).

raw data are reported (Fig. 3) along with spline interpolation for a 5 m we long ice section; the interpolation fits the original data well. Finally, we removed the mean concentration value.
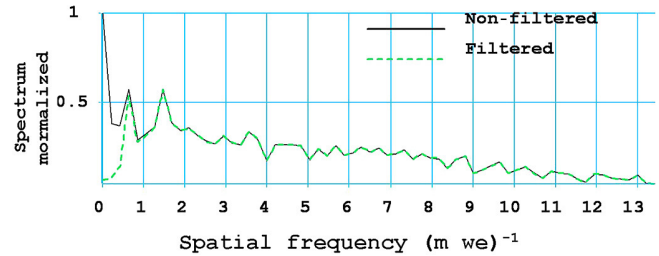
After spline re-sampling, thresholding, and mean value removal, we estimated the averaged concentration spectrum (Fig. 4). The low-frequency high level visible in Fig. 4 is due to the red character of geophysical noise. These dominant low frequencies would perturb the tracking of the spatial frequency by time–frequency analysis. They were eliminated by applying a high-pass filter of cut-off frequency f_b. The spatial low-frequency estimate is sensitive to the value of this cut-off frequency. Section 4.2.4 explains how the cut-off frequency was optimized using volcanic markers.

The normalized new concentration obtained after this pre-processing is called $S_X(l)$, where X is the component under investigation and l is the sample index (l varying from 1 to 2048). $S_{\mathrm{NO_3^-}}(l)$ is presented in the left part of Fig. 5 for the whole core, and in the right part for the specific sections determined in Fig. 1a, b, and c. The comparison of Figs. 1 and 5 shows that pre-processed concentrations correctly follow the initial concentration profile.

The sampling period P_s resulting from the spline interpolation is

$$P_s = \frac{76.4}{2048} = 0.0373\,\mathrm{m\,we}. \tag{4}$$

This sampling period enables us to represent the concentration inside the spatial frequency band from 0 to the "Nyquist–

Shannon[2] spatial frequency", f_{NS}:

$$f_{\mathrm{NS}} = \frac{1}{2P_s} = 13.40\,(\mathrm{m\,we})^{-1}. \tag{5}$$

4.2 Estimate of the spatial frequency

The energy distributions of concentration profiles in the depth–spatial frequency plane were determined here using Fourier time–frequency analysis and wavelet transform. The time–frequency representation based on Fourier transforms leads to spectrograms. Wavelet transforms provide scalograms (Daubechies, 1990; Rioul and Duhamel, 1992). In the next section, we present spatial frequency estimates deduced first from the spectrogram and then from the scalogram.

4.2.1 Spectrogram and scalogram

The spectrogram was obtained by pre-windowing the signal around a given depth, calculating its Fourier transform, taking the square modulus, and doing the same for every depth. The spectrogram is given by

$$\mathrm{SPECT}_X(d, f_s) = |\sum_{l=0}^{N-1} S_X(l)h(l-d)e^{-2j\pi\frac{f_s l}{N}}|^2, \tag{6}$$

where $h(d)$ is a sliding window of length N (Hanning function). The layer thickness resolution of the spectrogram is determined by the length of the selected sliding window $h(d)$.

Two orthogonal Morlet wavelets (Goupillaud et al., 1985) with S successive compression factors (scales) were used to calculate the scalogram. At each depth and on each scale, we project the concentration $S_{\mathrm{NO_3^-}}$ onto the vector of the S orthogonal Morlet wavelets. The power on each scale is the

---

[2]The Nyquist–Shannon sample theorem tells us that a band-limited signal can be perfectly reconstructed from a countable sequence of samples if the band limit, $B = f_{\mathrm{max}}$, is no greater than half the sampling rate: $f_{\mathrm{NS}} > 2f_{\mathrm{max}}$. When the frequency signal f_{sig} is too high ($f_{\mathrm{sig}} > f_{\mathrm{max}}$), the reconstruction exhibits imperfections known as aliasing.
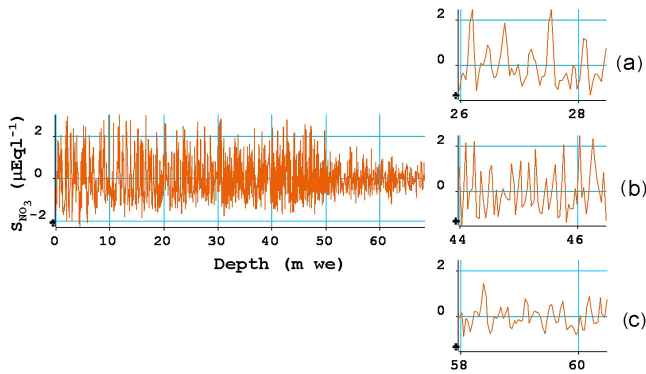
Figure 5. Same as Fig. 1, except S_{NO_3} (instead of c_{NO3}), which correspond to reprocessed nitrate concentration after thresholding, spline interpolation, and mean value removal.

Figure 6. Scalogram (top) and spectrogram (bottom) of NO_3 concentration depth profiles as a function of depth in m we and spatial frequencies f_s $((m\,we)^{-1})$. The colour scale (from blue to red) shows increasing energy of the concentration.

sum of the square of the projection onto the two orthogonal Morlet wavelets. This gives the power of the concentration signal on the depth-scale plane (depth-scale representation), from the relation between the scales and the spatial frequencies we got, by a spline transform of the scalogram in the depth–spatial frequencies plane called $SCAL_X(d, f_s)$.

Figure 6 shows the spectrogram (bottom) and the scalogram (top) of nitrate concentration in the depth–spatial frequency plane. The spectrogram is calculated for N consecutive samples. On the basis of successive tests, we determined that the best plots of the spectrogram were obtained for a window size of 128 samples corresponding to a layer thickness of 4.775 m we. For the scalogram we used $S = 35$ scales, which covers continuously the spatial frequency band of the concentration signal.

The depth trend of the energy main value, and thus of spatial frequency, is tracked by the green-blue "streak" on the spectrogram and scalogram shown in Fig. 6. Spatial frequency tends to increase from approximately $1\,(m\,we)^{-1}$ to $8\,(m\,we)^{-1}$ along the upper first 48 m we. This increase is consistent with annual layer thinning with depth due to ice flowing. Deeper than 48 m we, the spatial frequency, tracked by the green "streak", decreases. The trend reversal of the spatial frequency and its abnormal decrease below 48 m we (already visible in the raw concentration depth profile in Figs. 1 and 5) can be explained by spectrum aliasing, as we will explain in Sect. 4.2.5.

4.2.2 Estimate of the spatial frequency

Spatial frequency estimates from the spectrogram and the scalogram are given by the spatial frequency f_s of the spectrogram and scalogram maxima at each depth, d:

$$\widehat{f}_{s,spec}(d) = \max_{f_s}(SPECT_X(d, f_s)) \tag{7}$$

$$\widehat{f}_{s,scal}(d) = \max_{f_s}(SCAL_X(d, f_s)), \tag{8}$$
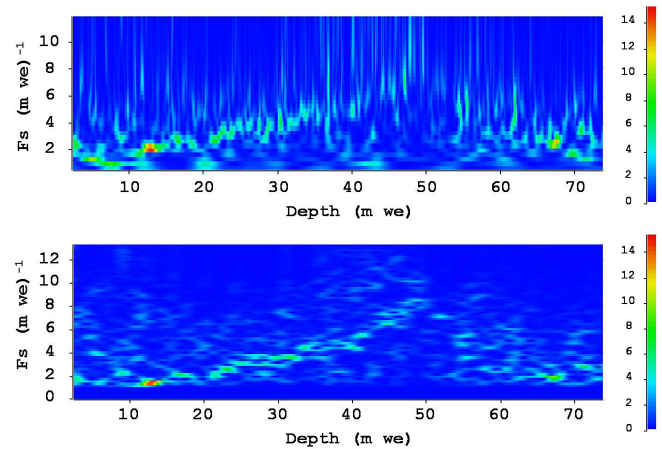
where $SPECT_X(d, f_s)$ and $SCAL_X(d, f_s)$ are the spectrogram and the scalogram corresponding to component X (here nitrate), and are expressed as functions of depth and spatial frequency.

In the upper part of Fig. 7, we show spatial frequencies estimated from the spectrogram (left) and the scalogram (right). Direct estimates of spatial frequency increase from 0 to 48 m we and then decrease due to spectrum replication and frequency aliasing. Aliasing is an artefact occurring when the signal reconstructed from samples is different from the original continuous signal. Here, the term refers to the higher frequencies becoming aliased and indistinguishable from the lower-frequency components in the signal when the sampling rate falls below the Nyquist–Shannon frequency. In other words, under-sampling causes high-frequency components to appear as spurious low frequencies. This issue is discussed in Sect. 4.2.5.

Discontinuities are visible in both panels of Fig. 7; however, their number is significantly greater in the scalogram estimate than in the spectrogram estimate. These discontinuities come from the dynamics of the signal, which is made up of successive events of short duration and varying amplitude, the occurrence of which is modulated by seasonal periodicity. It has been observed that the wavelets are very sensitive to short-duration events (Mallat et al., 1992). The greater number of discontinuities seen in the scalogram led us to consider that the spectrogram was a better tool than the scalogram for tracking the spatial frequency in the concentration signal.

4.2.3 Discontinuity correction with a median filter

We have used a median filter of length $M = 2m + 1$ to eliminate the discontinuities in spatial frequency estimates, $\widehat{f}_s(d)$ (Coquerez et Philipp, 1995).
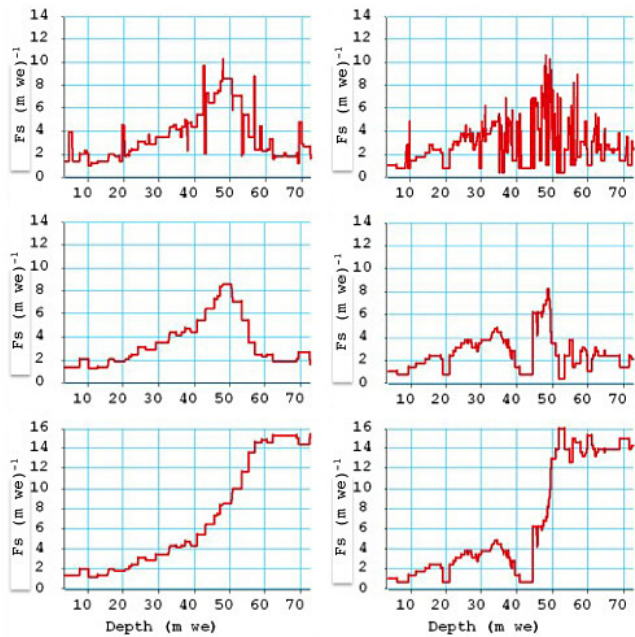
Figure 7. Estimate of the spatial frequency associated with annual layer thickness as a function of depth from the spectrogram (left column) and scalogram (right column). Top: direct estimate; middle: estimate after application of the median filter; bottom: estimate after application of the median filter and de-aliasing.

The output of median filters applied to the spatial frequency estimates, $\widehat{f_s}(d)$, provided by the spectrogram and the scalogram is given by

$$\mathrm{MF}[\widehat{f_s}(d)] = \mathrm{median}\{\widehat{f_s}(i), i \in [d-m, d+m]\}. \qquad (9)$$

The results of the median filter application are shown in Fig. 7 (middle panels).

4.2.4   Filter optimization

In the pre-processing step (see Sect. 4.1), we introduced a high-pass filter with a cut-off frequency, f_b. Here we utilized a median filter of length M. To determine the optimum values of the high-pass filter cut-off frequency, f_b, and the median filter length, M, we used two volcanic references: the depths where the volcanic debris attributed to tropospheric deposits from the Pinatubo and Mount Agung eruptions were found (de Angelis et al., 2003). The Tambora eruption was not taken into account because the corresponding layer was located below the aliasing depth.

Eruption dates were calculated for the following set of f_b and M values:

$$f_b = (0,2 + 0,1\,p) \qquad (10)$$
$$p = [0,2,\ldots,10] \qquad (11)$$
$$M = [17,33,65] \qquad (12)$$

The optimum values of f_b and M are the ones that minimize the distance between estimated and historical eruption dates using the criterion

$$\widehat{F}_{(f_b, M)} = |D_{(\mathrm{Pin})} - \widehat{D}_{(\mathrm{Pin})}(f_b, M)| \qquad (13)$$
$$+ |D_{(\mathrm{Agu})} - \widehat{D}_{(\mathrm{Agu})}(f_b, M)|,$$

where $D_{(\mathrm{Pin})}$ and $D_{(\mathrm{Agu})}$ are the true eruption dates for Pinatubo and Mount Agung, respectively, and $\widehat{D}_{(\mathrm{Pin})}(f_b, M)$ and $\widehat{D}_{(\mathrm{Agu})}(f_b, M)$ are the estimated dates obtained by combining the parameters (f_b, M).

Once applied to $S_{\mathrm{NO_3^-}}$ spatial frequencies estimated with the spectrogram and the scalogram, the optimization procedure led to the following optimum values.

Spectrogram estimate:

$$f_b = 1.1\,(\mathrm{m\,we})^{-1} \text{ and } M = 65 \qquad (14)$$

Scalogram estimate:

$$f_b = 0.2\,(\mathrm{m\,we})^{-1} \text{ and } M = 65 \qquad (15)$$

In the middle panels of Fig. 7, we show the spatial frequency estimated with the spectrogram (left) and the scalogram (right) as a function of depth obtained with the optimum values of f_b and M. Discontinuities are smoothed in the two plots. Their attenuation is more efficient in the spectrogram estimate than in the scalogram estimate.

4.2.5   Evidence of spectrum replication

The initial core sampling was continuous: the core was cut into 1697 successive ice sections and analyses were performed of every ice section once melted. This analytical procedure is equivalent to an averaging sampler. The length d_{slices} of each sample which gives the sampling period changes with depth. At this experimental length, we associate a "chemical Nyquist–Shannon frequency" f_{chem}:

$$f_{\mathrm{chem}} = \frac{1}{2 \times d_{(\mathrm{slices})}}. \qquad (16)$$

We present in Fig. 8 the "Chemical Shannon frequency" (dark line) corresponding to the true core sampling, the "Spline Shannon frequency" (dark dotted line) corresponding to the regular resampling applied to the original data (see Sect. 4.1), and the spatial frequency estimate obtained previously and corresponding to the one-year periodicity expected for the data (called "One-year frequency" and denoted by a green line).

Three distinct parts can be distinguished in Fig. 8. From 0 to approximately 35 m we (Part 1), the "effective" Nyquist–Shannon frequency, which is the lowest of the two Nyquist–Shannon frequencies reported in Fig. 8, is the chemical one, and the "One-year frequency" is not aliased. From 35 to 50 m we (Part 2), the "effective" Nyquist–Shannon frequency
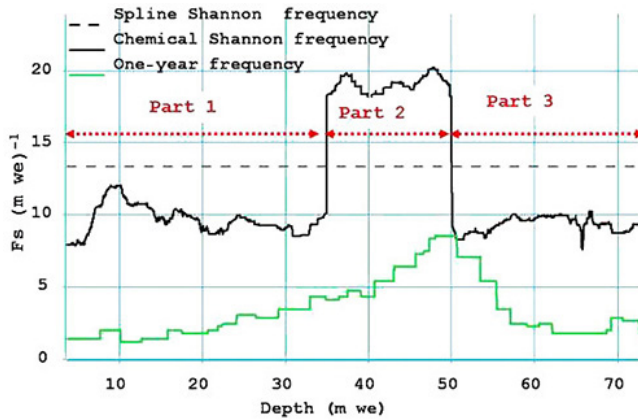
Figure 8. Nyquist–Shannon frequency deduced from the true core sampling ("Chemical Shannon frequency", dark line); Nyquist–Shannon frequency deduced from the spline pre-processing ("Spline Shannon frequency", dark dotted line); estimated spatial frequency provided by the spectrogram ("One-year frequency", green line).

Figure 9. Illimani chronologies deduced from the NO_3 concentration depth profile and using the spectrogram (black line) and the scalogram (green line).

is the "Spline Shannon frequency". In this region the "One-year frequency" remains non-aliased. At 50 m we, we observe that the effective Nyquist–Shannon frequency is again the "Chemical Shannon frequency", and that the increasing "One-year frequency" becomes equal to the "Chemical Shannon frequency", and then decreases (Part 3).

The increase in the "One-year frequency" observed between 0 and 50 m we results from annual layer thinning with depth due to ice flow. Given that the influence of this thinning effect increases with depth and is certainly stronger below 50 m we than above it, we can conclude that the decreasing trend of the one-year frequency observed below 50 m we is an artefact due to spectrum replication.

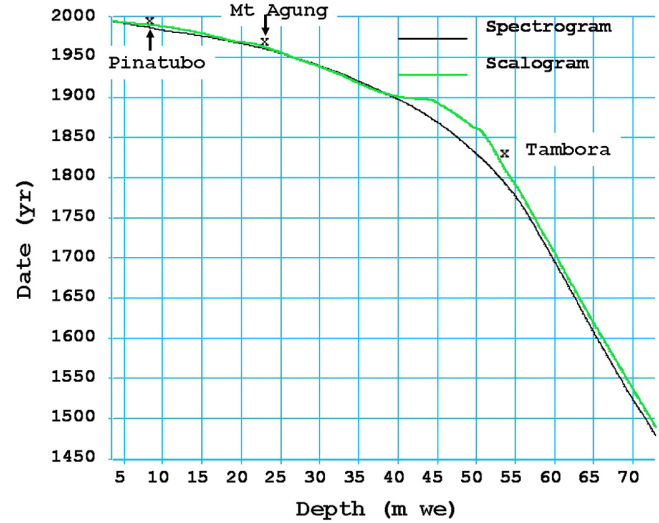#### 4.2.6   Correcting the aliasing: de-aliasing

In order to recover the non-aliased value of the one-year frequency $f_s(d)$ as a function of depth d, we replaced the observed (aliased) one-year frequency $f_a(d)$ below the crossing depth, i.e. the depth ($d_{crossing}$) where aliasing occurs, with

$$f_s(d) = 2 \times f_C(d) - f_a(d), \tag{17}$$

where $f_s(d)$ is the non-aliased one-year frequency, $f_C(d)$ the "Chemical Shannon frequency", and $f_a(d)$ the "observed aliased frequency".

De-aliasing requires one to determine as accurately as possible $d_{crossing}$, which is the depth where one-year spatial frequency and chemical Nyquist–Shannon frequency cross. Given the discontinuous nature of the data, $d_{crossing}$ was estimated as follows:

$$d_{crossing} = \text{Argmin} |f_C(d) - f_s(d)|. \tag{18}$$

Spatial frequency estimates from the spectrogram and the scalogram after de-aliasing are presented in Fig. 7 (bottom left and right panels, respectively).

5   Chronology deduced from nitrate (NO_3^-) concentration depth profile and accuracy analysis

5.1   Chronology deduced from nitrate (NO_3^-)

From Eq. (3), the estimate of the time delay between the depth origin of the determination of the spatial frequency, d_{min}, and the date corresponding to the depth d is

$$\widehat{t}(d) = \int_{d_{min}}^{d} \widehat{f}_s(u) du + \widehat{t}(d_{min}), \tag{19}$$

– where d_{min} coming from the windows of the spectrogram (N samples) and the median filter (M samples) is

$$d_{min} = \left(\frac{N+M}{2}\right) P_s = 3.6 \, \text{m we}, \tag{20}$$
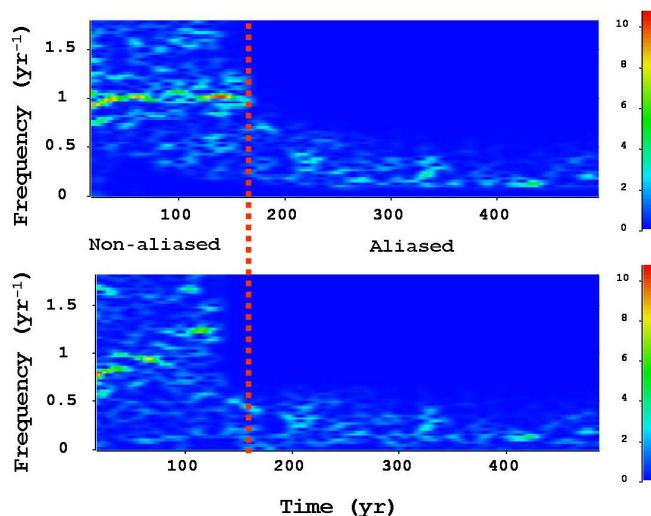
– and $\widehat{t}(d_{min})$ is

$$\widehat{t}(d_{min}) = \widehat{f}_s(d_{min} d_{min}). \tag{21}$$

The date corresponding to the depth d is

$$\widehat{date}(d) = d_{drill} - \widehat{t}(d). \tag{22}$$

The chronologies derived respectively from the nitrate spectrogram and scalogram are shown in Fig. 9. The drilling

Figure 10. Spectrograms of S_{NO_3} as a function of the time delay estimate $\hat{t}$. The time delay estimate $\hat{t}$ is given by the chronology deduced from the spectrogram (top) and the scalogram (bottom). The red dotted vertical line indicates the time corresponding to the aliasing.

date d_{drill} was fixed at AD 1999. Both chronologies are globally coherent, but local discrepancies are visible, particularly between 40 m we and 55 m we. This raises the key question of the chronology's reliability.

5.2 Evaluation of the chronology inferred from the NO$_3^-$ concentration depth profile

Evaluating the chronology's reliability (accuracy) is a key step towards validating our method. For that, we propose three approaches. The first approach refers only to our chronology. In the second approach, we use the volcanic markers. Finally, we compare our chronology with the independent year-by-year chronology used by de Angelis et al. (2003) and Correia et al. (2003) for the upper part of the core.

5.2.1 Direct evaluation of our method

We have determined the time delay estimates, $\hat{t}(d)$, with the spectrogram and the scalogram. From the pre-processed nitrate concentration depth profile $S_{NO_3^-}(d)$ and the time delay estimates $\hat{t}(d)$ given by the two chronologies, resulting respectively from Fourier time–frequency and wavelet transforms, and using a spline transformation, we got the concentration of NO$_3^-$ as a function of the time delay estimate: $S_{NO_3^-}(\hat{t})$.

The spectrograms of $S_{NO_3^-}(\hat{t})$, corresponding respectively to Fourier time–frequency (spectrogram, top panel) and wavelet (scalogram, bottom panel) transforms, are presented in Fig. 10. These spectrograms show two very different parts:

before and after 160 yr before the drilling date, i.e. before AD 1999.

The part of the spectrograms corresponding to time delay values greater than 160 yr are associated with the aliased part of the data and, due to the aliasing, all energies are concentrated at frequencies lower than 1 yr^{-1}. Thus, we did not use this part of the spectrograms to check the quality of our method.

For time delay values lower than 160 yr, i.e. the non-aliased part of the data, the spectrogram of $S_{NO_3^-}(\hat{t})$ deduced from the dating with the spectrogram (top panel) clearly shows a track centered at 1 yr^{-1}. This indicates that the results of the Fourier time–frequency are in agreement with our working hypothesis that aimed to find a seasonal triggering in the nitrate concentration depth profile. On the opposite end, no trend (scattered values ranging from 0.8 yr^{-1} to 1.2 yr^{-1}) is visible between the origin and 160 yr on the spectrogram of $S_{NO_3^-}(\hat{t})$ resulting from the dating with the scalogram (bottom panel). This strongly suggests that wavelet transforms cannot be used to detect seasonal variations in our data set unambiguously.

5.2.2 Evaluation of the chronologies deduced from the NO$_3^-$ depth profile by comparison with volcanic tie points

The historical dates of Pinatubo, Mount Agung and Tambora tropospheric plume arrivals and corresponding dates deduced from the use of the spectrogram ("Date 1") and the scalogram ("Date 2"), and from the annual layer counting by de Angelis et al. (2003) ("Date 3"), are given in Table 1. As a general rule, specific attention must be paid to the use of volcanic eruptions as tie points for the dating of Andean ice cores. Major volcanic eruptions can be clearly identified in Antarctic ice cores through the arrival of large amounts of sulfuric acid from the stratosphere. However, the formal identification of a given individual event requires specific micro-physical and micro-chemical investigations of ashes to be confirmed, unless detailed matching with another well-dated ice core can be provided. In tropical South America, the quiescent or eruptive activity of Andean volcanoes competes with the influence of eruptions taking place farther north in the tropical belt. Combined with the lack of information on dispersion and removal parameters, as well as on the relative importance of tropospheric transport and stratosphere–troposphere exchanges, this makes uncertain the use of general volcanic markers alone in relating a given peak to a given eruption. Nevertheless, it must be noted that the depth corresponding to the plume arrival attributed to the Mount Agung eruption is in agreement with $^{37}C_s$ and tritium peaks at 33.5 m (21.7 m we) associated with stratospheric fallout in 1964 of major nuclear bomb tests performed in the Northern Hemisphere.

The dates obtained for the Pinatubo and Mount Agung eruptions with the two approaches used in this study are very

Table 1. Dating of tie points issued from the spectrogram and the scalogram, and published by de Angelis et al. (2003). Differences in Tambora eruption dates may be due to the fact that this eruption is located in the aliased part of the data or due to inaccurate eruption identification.

Eruption	Pinatubo	Mount Agung	Tambora
Historical date	1991.5	1963.3	1815
Date 1 (spectrogram)	1990.9 (−0.6)	1962.4 (−0.87)	1794.1 (−21)
Date 2 (scalogram)	1991.3 (−0.2)	1964.2 (0.94)	1812.5 (−2.5)
Date 3 (multi-parameter counting)	1991.7	1963.8	–

Figure 11. Comparison between the chronology established by de Angelis et al. (2003) and chronologies proposed in this article using $S_{NO_3^-}$ with the spectrogram (left) and the scalogram (right).

close to the eruptions' historical dates. We keep in mind that these reference horizons have been used to optimize the high-pass filter cut-off frequency and the median filter length, so it is normal to recover these historical dates approximately. However, the results presented in Table 1 provide a valuable estimate of the overall precision of every dating method. The dates deduced from the spectrogram and the scalogram for the arrival of volcanic debris observed at 53.51 m we and attributed to the Tambora eruption by de Angelis et al. (2003) are different from the historical date, i.e. 1815[3]. These differences may be due to the fact that this eruption is located in the aliased part of the data, but they must also be considered keeping in mind chronological discrepancies between previous studies related to the choice of more accurate time references. The chronology of a nearby ice core based on the counting of pseudo-seasonal layers and the location of major peaks in the electrical conductivity profile (Knüsel et al., 2003) locates at 99.9 m we the arrival of a major unknown eruption dated to AD 1258 in Antarctica. The choice of this volcanic anchor layer appeared to be congruent with visual counting. However, this chronology was largely reassessed by Kellerhals et al. (2010). Considering thallium as an unambiguous volcanic marker, these authors used the location of major thallium peaks combined with ice modelling and preliminary ^{14}C data to locate the AD 1258 horizon at 90.7 m we, i.e. 9.2 m we higher, which implies a gap of more than 300 yr between both chronologies, and underlines the potential bias induced by subjective factors in the visual identification of the annual layer approach and the choice of tie points.

5.2.3 Comparison with a year-by-year multi-proxy counting approach

We now compare the timescales, deduced respectively from the $S_{NO_3^-}$ spectrogram and scalogram for the upper part of
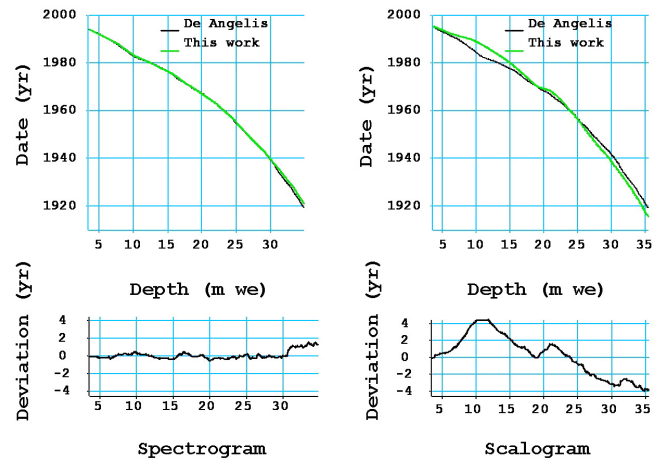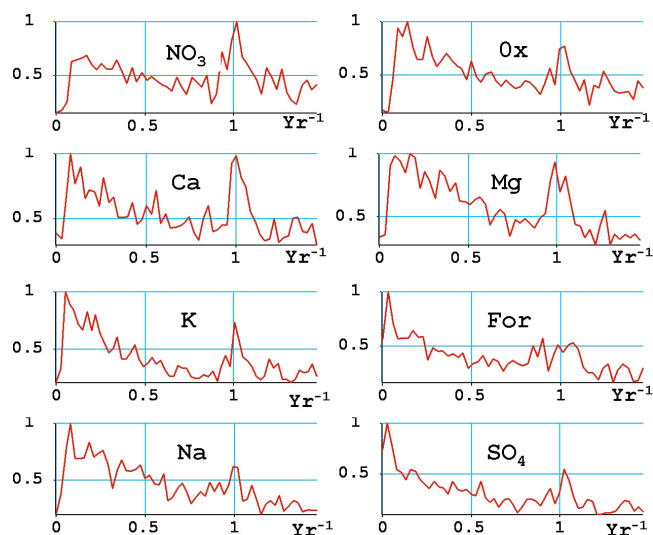
the core (0–36.4 m we) with the chronology inferred from the multi-proxy year-by-year dating approach proposed by de Angelis et al. (2003).

The timescale published in 2003 for the upper part of the core (de Angelis et al., 2003) is represented by a black line in the upper part of Fig. 11 (top panels), while timescales, deduced respectively from the $S_{NO_3^-}$ spectrogram (left) and scalogram (right), are represented by a green line (this work). The corresponding differences are presented in the bottom part of the figure. The date gap corresponding to the spectrogram (left panel) remains close to zero from the signal analysis origin depth to 30 m we. It increases slightly deeper down, reaching 1.5 yr at 35 m we. The chronological deviation corresponding to the scalogram (right panel) is higher, particularly between 5 and 15 m we, and reaches 4 yr at 10 m we.

5.2.4 Conclusion on the application of Fourier time–frequency and wavelet transforms to the NO_3^- concentration depth profile

In the previous sections, we presented (1) a direct evaluation of our chronology, (2) a comparison of the dates deduced from spectrogram and scalogram analysis for volcanic layers attributed to well-known cataclysmic eruptions and the true eruption dates, and (3) a comparison of timescales provided by scalogram and spectrogram analysis with a previously published chronology based on a multi-proxy year-by-year counting approach.

This allows us to conclude that our method provides chronologies consistent with the available information. However, the seasonal variability of nitrate concentrations is clearly identified only when using the Fourier time–frequency transform. Moreover, the chronology deduced from the spectrogram shows a better general agreement with the timescale published by de Angelis et al. (2003) than the

---

[3]The closeness of the Tambora datation by the scalogram comes from an artefact introduced by the estimation of spatial frequency between 40 and 45 m we (Fig. 7, bottom-right panel).

Figure 12. Spectra (in yr^{-1}) of nitrate (NO_3), oxalate (Ox), calcium (Ca), magnesium (Mg), potassium (K), formate (For), sodium (Na), and sulfate (SO_4) concentration depth profiles as a function of time delay estimate.

chronology inferred from the scalogram. As shown in Fig. 7, this may be explained by the greater rate of discontinuities introduced when estimating spatial frequencies from the scalogram. It is not relevant to evaluate the quality of our method in the aliased part of the data directly. We are aware that the Tambora eruption is dated inaccurately. Nevertheless, we were able to detect spectrum aliasing due to the sampling procedure, to reverse the aliasing, and to propose a preliminary timescale.

At this stage, we may reasonably consider that this timescale, although less accurate below the aliasing depth than what may be expected from high-resolution concentration depth profiles, has more reliability than dating based on the search for annual layers along under-sampled ice sequences. Indeed, it can be seen in Fig. 1c that annual layer thickness seems notably to increase in the deeper part of the core, which is inconsistent with ice flow considerations upstream of the Illimani drilling site (Kellerhals et al., 2010). As clearly evidenced when comparing Fig. 7 (top panel) and Fig. 7 (bottom panel), this is an artefact: without de-aliasing, the annual layer thickness progressively re-increases from approximately 10 cm we at 48 m we to more than 30 cm we below 60 m we, while it continues to decrease to less than 7 cm we below 60 m we once spectrum aliasing has been corrected. In light of these observations, the dating proposed by Ramirez et al. (2003) for the same core section should likely be partly reassessed: indeed, these authors considered seasonal layer counting to be possible down to 66 m we, but used a mean sample length of 5.8 cm we, i.e. greater than the length required to avoid aliasing. As a consequence, the age difference of 68 yr found between the Tamb-

ora layer (53.5 m we, sulfate peak used as an absolute tie point) and 66 m we (AD 1747 ± 20 yr), which corresponds to a mean annual layer thickness of 18 cm we, should be significantly underestimated. Furthermore, the uncertainty of ±20 yr based only on cumulative error related to questionable layers, and failing to take into account under-sampling problems, is not relevant.

We have validated our method by comparing our dating with the year-by-year counting supporting by volcanic tie points published by Correia et al. (2003) and de Angelis et al. (2003). Nevertheless, the accuracy of any dating method cannot be assessed if other dating tools are not available, and only the consistency between independent approaches can definitely support the final chronology. The new method presented here contributes to such a cooperative approach.

In the next section, the spectrogram is applied to concentration depth profiles of seven other ions, making it possible to compare and discuss the suitability of each ion as a dating proxy.

6 Comparison of ion variability and suitability for ice core dating

The seven ions studied here and compared with nitrate (NO_3^-) are sulfate (SO_4^{2-}), sodium (Na^+), calcium (Ca^{2+}), magnesium (Mg^{2+}), potassium (K^+), oxalate (Ox), and formate (For). They were chosen for the reservoirs they are expected to originate from and for their emission seasonality. The soluble part of continental input at the Illimani site is mainly regional, and consists of gypsum ($CaSO_4$) and halite (NaCl). Strong acidic gases of volcanic origin react with wind-blown minerals and volcanic ashes, leading to the formation of secondary gypsum, halide salts, and lower amounts of other sodium, magnesium and potassium salts. Halite may also originate from the large salars present in northern Chile and Bolivia, mostly during the dry season. In tropical South America, the fire season occurs during the dry season. Fire events recorded along the Illimani ice core were identified by simultaneous peaks of ammonium, formate and nitrate, and significant amounts of soluble potassium (de Angelis et al., 2008). Local emissions of nitrate and ammonium by soils, and formate by vegetation, may also be expected to be more likely during the warm wet season. Oxalate is directly emitted through biomass burning, but may also be produced through the oxidation of volatile organic compounds (VOC) scarcely investigated in the South American atmosphere.

6.1 Optimization

In the pre-processing step, we have thresholded the concentration of seven ions at 0.98 level in the cumulative distribution function. Optimal values of the high-pass filter cutoff frequency f_b and the median filter length M were determined for the seven new ions using the criterion presented
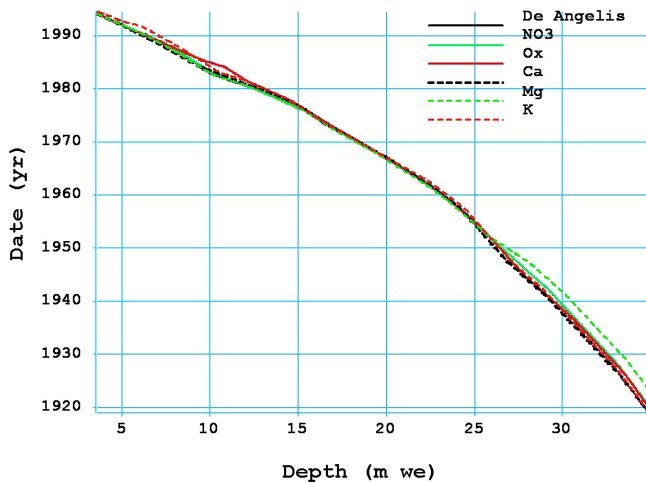
Figure 13. Comparison of chronologies deduced from nitrate (NO$_3$), oxalate (Ox), calcium (Ca), magnesium (Mg), and potassium (K) concentration profiles with the chronology established by de Angelis et al. (2003).

in Sect. 4.2.4, with reference to Pinatubo and Mount Agung eruption dates. The results of the optimization procedure are summarized in Table 2, along with the corresponding minimum value of $\widehat{F}(f_b, M)$ defined in Eq. (13). We also specify if the 1 yr^{-1} frequency was clearly found in the corresponding concentration spectra expressed as a function of the time delay estimate (see Fig. 12, where concentration spectra are expressed as a function of time estimated for the eight ions). The eight ions are sorted according to ascending values of the distance criterion $\widehat{F}(f_b, M)$. Peaks corresponding to annual frequency are clearly visible in the nitrate, oxalate, calcium, magnesium and potassium panels in Fig. 12. This is not similar for sulfate, sodium and formate, and is consistent with the sorting presented in Table 2 according to the quality criterion. All that makes it possible to estimate experimentally the relative quality of chronologies based on each concentration depth profile.

6.2 Chronology overall comparison

A preliminary interpretation of signal analysis in terms of time marker reliability may be extracted from Fig. 13, where time–depth relationships, deduced respectively from NO$_3^-$, Ox, Ca^{2+}, Mg^{2+} and K$^+$ concentration profiles, are shown along with the time–depth relationship used by de Angelis et al. (2003). A rather good consistency between the five chronologies proposed here as well as with the chronology used by de de Angelis et al. (2003) is observed down to ca. 28 m we, i.e. from the late 1950s to the date corresponding to the signal origin depth. A more detailed representation of chronology trends may be found in Fig. 14, which shows the deviation of our eight independent chronologies from the chronology of de Angelis et al. (2003). Nitrate and

calcium provide the best compatibility with the chronology published by de Angelis et al. (2003) and the two volcanic tie points. This confirms our hypothesis that these two ions are produced during the dry season: nitrate production is largely dominated by biomass burning compared with soil emission during the warm season, and wind-blown soil dust is by far the most important source of soluble calcium, the relative contribution of volcanic ash remaining low. The good performance of oxalate, both in terms of seasonality and dating accuracy, is very likely due to enhanced production through biomass burning combined with heterogeneous uptake on mineral dust during the dry season, as supported by deviation similarities in calcium and oxalate curves. Several mechanisms related to emission and/or transport processes may have contributed to disturbing the signal seasonality of the other ions. Like calcium, magnesium and the part of potassium not related to biomass burning come mainly from erodible soil dust emission, with a sporadic volcanic contribution. However, the composition and dissolution rate of soil dust and volcanic ashes vary depending on soil and eruption types, which influence the signal of the less soluble species (i.e. magnesium and potassium) in a more significant way than the signal of the more soluble ones like calcium. Episodic transport of polluted plumes of local origin through convection during the wet season since the mid-1950s in addition to the timing of stratospheric volcanic arrivals are very likely responsible for the absence of a clear 1 yr^{-1} frequency in the sulfate profile and corresponding ice age overestimate. Similarly, the occurrence of non-periodic peaks related to halite formation and to partial dissolution of ashes in volcanic plumes may become significant compared with seasonal sodium emission from salars, and may thus explain the bad performance of this ion. Although largely related to biomass emissions, the formate signal does not show the 1 yr^{-1} frequency as clearly visible on the nitrate spectrum. If deposited as ammonium or nitrate salt, formate should covary with nitrogen species, while, if deposited as formic acid, it becomes sensitive to post-deposition processes, including peak removal from strongly acidic layers and relocation on mineral particles.

7 Conclusions

The main results highlighted from the present study are as follows: spectral analysis applied here to ion depth profiles gained along a tropical ice core (the Illimani summit area) appears to be a potential dating tool that does not require preliminary knowledge of the net accumulation rate or ice flow characteristics. When applied to the nitrate concentration depth profile, both Fourier time–frequency and orthogonal Morlet wavelet transforms allow the determination of the spatial frequency as a function of depth.

Spectrum replication due to analytical under-sampling was detected below 48 m we in this core on both the scalogram
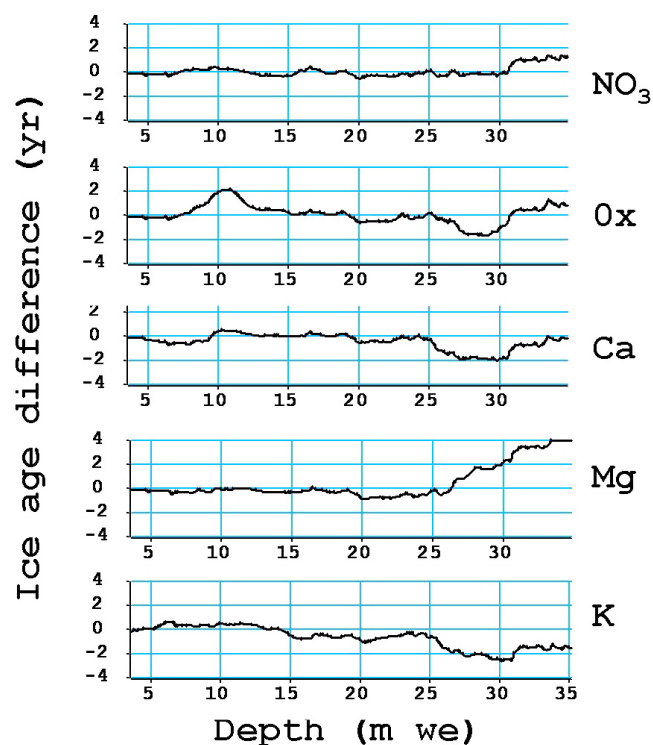
Figure 14. Ice age differences (yr) calculated for the 36 upper metres (m we) between the chronology given by de Angelis et al. (2003) and chronologies deduced from nitrate (NO$_3$), oxalate (Ox), calcium (Ca), magnesium (Mg), and potassium (K) concentration profiles (from top to bottom, respectively).

Table 2. Comparison of nitrate, oxalate, calcium, magnesium, potassium, formate, sodium, and sulfate (from top to bottom, respectively), in terms of dating suitability.

Concentration	Frequency f_b	Filter length M	Min $\widehat{F}_{(f_b, M)}$	Retrieve 1 year
NO$_3^-$	1.1	65	0.27	Yes
Ox	0.9	65	0.39	Yes
Ca^{2+}	1	65	0.47	Yes
Mg^{2+}	0.7	65	0.66	Yes
K$^+$	0.7	65	1.06	Yes
For	0.2	17	1.25	No
Na$^+$	0.6	17	4.65	No
SO$_4^{2-}$	0.2	33	6.09	No

We can conclude that Fourier time–frequency analysis applied to concentration depth profiles of selected atmospheric markers may be particularly suitable for establishing and comparing ice core chronologies at poorly documented sites. This analysis method will also be useful at sites where the dynamics of seasonal signals is significantly influenced by source proximity or regional meteorological features, for instance when emissions of local or regional origin make it difficult to locate unambiguously specific events of global importance or anthropogenic trends commonly used as adjusting marks along polar ice cores.

The Supplement related to this article is available online at doi:10.5194/cp-10-1659-2014-supplement.

and the spectrogram. This aliasing effect occurs when the spatial frequency becomes greater than the experimental Nyquist–Shannon frequency imposed by the initial chemical sampling procedure. It significantly increases the difficulties encountered in core dating, and prevents us from directly assessing the chronological accuracy along the aliased part of the data. Nevertheless, we are able to propose a de-aliasing method that certainly improves the ice core chronology in comparison with manual counting of pseudo-annual layers in the under-sampled part of the core. Above the aliasing depth, the chronology provided by the Fourier time–frequency analysis is in close congruence with the chronology based on multi-proxy year-by-year counting of wet season minima adjusted with the Pinatubo and Mount Agung eruption dates. Wavelet transforms appear to be less efficient than Fourier time–frequency analysis for concentration signals characterized by a wide dynamic range and the occurrence of sporadic events.

Once applied to the concentration profiles of seven other ions considered as potential source markers, Fourier transform analysis provides eight independent chronologies and preliminary information on the natural variability of the cycles of each of these ions.

References

Andersen, K. K., Svensson, A., Johnsena, S. J., Rasmussena, S. O., Biglera, M., Rothlisbergerb, R., Ruthc, U., Siggaard-Andersen, M. A., Steffensen, J. P., Dahl-Jensena, D., Vinthera, B. O., and Clausena, H. B.: The Greenland Ice Core Chronology 2005, 1542 ka. Part 1: constructing the time scale, Quat. Sci. Rev., 25, 3246–3257, 2006.

Cohen, L.: Time frequency Analysis: Theory and applications, Prentice Hall Professional Technical Reference, December 1994.

Coquerez, J.-P. and Philipp, S.: Analyse d'images: filtrage et segmentation, Masson, 1995.

Correia, A., Freydier, R., Delmas, R. J., Simões, J. C., Taupin, J.-D., Dupré, B., and Artaxo, P.: Trace elements in South America aerosol during 20th century inferred from a Nevado Illimani

ice core, Eastern Bolivian Andes (6350 m a.s.l.), Atmos. Chem. Phys., 3, 1337–1352, doi:10.5194/acp-3-1337-2003, 2003.

Daubechies, I.: The wavelets transform, time frequency localization and signal analysis, IEEE Trans. on Info. Theory, IT-36(5) 961–1005, September 1990.

De Angelis, M., Simées, J., Bonnaveira, H., Taupin J. D., and Delmas, R. J.: Volcanic eruptions recorder in the Illimani ice core (Bolivia): 1918–1998 and Tambora periods, Atmos. Chem. Phys., 3, 1–37, 2003,
http://www.atmos-chem-phys.net/3/1/2003/.

De Angelis, M., Ginot, P., and Moreno, I.: Continental biomass influence in the free troposphere from tropical South America to Patagonia: Seasonal and long term variability inferred from three high altitude Andean ice cores 10th IGAC Conference "Bridging the Scales in Atmospheric Chemistry: Local to Global" 7 to 12 september 2008, Annecy, France, 2008.

Flandrin, P.: Temps fréquence, Hermés, Paris, 1993.

Goupillaud, P., Grossmann, A., and Morlet, J.: Cycle octave related transform processing in seismic signal analysis, Geoexploration, 23, 85–102, 1985.

Kellerhals, T., Tobler, L., Bratsch, S., Sigl, M. , Wacker, L., Gaeggler, H. W., and Schwikovski, M.: Thallium as a Tracer for Preindustrial Volcanic Eruptions in an Ice core Record from Illimani, Bolivia, Environ. Sci. Technol., 44, 888–893, 2010.

Knusel, S., Ginot P., Schotterer U., Schwikowski M., Gäggeler H. W., Francou B., Petit J.-R., Simoes J. C., and Taupin J.-D.. Dating of two nearby ice cores from the Illimani, Bolivia J. Geophys. Res., 108, 4181–4190, 2003.

Lemieux-Dudon, B., Blayo, E., Petit, J. R., Waelbroeck, C., Svensson, A., Ritz, C., Barnola, J. M., Narcisi, B. M., and Parrenin, F.: Consistent dating for Antarctic and Greenland ice cores, Quat. Sci. Rev., 29, 8–20, 2010.

Mallat, S. and Hwang, W. L.: Singularity detection and processing with wavelets , IEEE Trans. on Info. Theory, proc. SP-40, 1746–1757, 1992.

Meese, D. A., Gow, A. J., Grootes, P., Stuiver, M,. Mayewski, P.A. Zielinski, G.A., Ram, M., Taylor, K. C., and Waddington, E. D.: The Accumulation Record from the GISP2 Core as an Indicator of Climate Change Throughout the Holocene, Science, 266, 1680–1682, 1997.

Narcisi, B., Petit, J. R., Delmonte, B., Basile-Doelsch, I., and Maggi, V.: Characteristics and sources of tephra layers in the EPICA-Dome C ice record (East Antarctica): implications for past atmospheric circulation and ice core stratigraphic correlations, Earth Planet. Sci. Lett., 293, 253–265, 2005.

Ramirez, E., Hoffmann, G., Taupin, J. D., Francou, B., Ribstein, P., Caillon, N., Ferron, F. A., Landais, A., Petit, J. R., Pouyaud, B., Schotterer, U., Simoes, J. C., and Stievenard, M.: A new Andean deep ice core from Nevado Ilimani (6350 m) Bolivia, Earth Planet. Sci. Lett., 212, 337–350, 2003.

Rasmussen, S., Seierstad, I., Andersen, K., Bigler, M., Dahl-Jensen D., and Johnsen S.: Synchronization of the NGRIP, GRIP, and GISP2 ice cores across MIS 2 and paleoclimatic implications, Quat. Sci. Revi., 27, 18–28, 2008.

Rioul, O. and Duhamel, P.: Fast algorithms for discrete and continuous wavelet transforms. IEEE Trans. Info. Theory, 39, 569–586, 1992.

Ruth, U., Barnola, J.-M., Beer, J., Bigler, M., Blunier, T., Castellano, E., Fischer, H., Fundel, F., Huybrechts, P., Kaufmann, P., Kipfstuhl, S., Lambrecht, A., Morganti, A., Oerter, H., Parrenin, F., Rybak, O., Severi, M., Udisti, R., Wilhelms, F., and Wolff, E.: "EDML1": a chronology for the EPICA deep ice core from Dronning Maud Land, Antarctica, over the last 150 000 years, Clim. Past, 3, 475–484, doi:10.5194/cp-3-475-2007, 2007.

Schotterer, U., Grosjean, M., Stichler, W., Ginot, P., Kull, C., Bonaveira, H., Francou, B., Gaggeler, H. W., Gallaire, R., Hoffmann, G., Pouyaud, B., Ramirez, E., Schwikowski, M., and Taupin, J. D.: Glaciers and climate in the Andes between the Equator and 30° S: What is recorded under extreme environmental conditions?, Clim. Change, 59, 157–175, 2003.

Smith, C. L., Fairchild, I. J., Spotl, C., Frisia, S., Borsato, A., Moreton, S. G., and Wynn, P. M.: Chronology building using objective identification of annual signals in trace element profiles of stalagmites, Quat. Geochronol., 4, 11–21, 2009.

Svensson, A., Nielsen, S.W., Kipfstuhl, S., Johnsen, S., J., Steffensen, J. P., Bigler, M., Ruth, U., and Röthlisberger, R.: Visual stratigraphy of the North Greenland Ice Core Project (North-GRIP) ice core during the last glacial period, J. Geophys. Res., 110, D02108, doi:10.1029/2004JD005134, 2005.

Svensson, A., Andersen, K. K., Bigler, M., Clausen, H. B., Dahl-Jensen, D., Davies, S. M., Johnsen, S. J., Muscheler, R., Parrenin, F., Rasmussen, S. O., Röthlisberger, R., Seierstad, I., Steffensen, J. P., and Vinther, B. M.: A 60 000 year Greenland stratigraphic ice core chronology, Clim. Past, 4, 47–57, doi:10.5194/cp-4-47-2008, 2008.

Thompson, L. G., Davis, M. E., Mosley-Thompson, E., Sowers, T. A., Henderson, K. A., Zagrodnov, V. S., Lin, P.-N., Mikhalenko, V. N., Campen, R. K., Bolzan, J. F., Cole-Dai, J., and Francou, B.: A 25 000-Year tropical Climate History from bolivian Ice Cores, Science, 282, 1858–1864, 1998.

Thompson, L. G., Mosley-Thompson, E., Davis, M. E., Lin, P.-N., Henderson K., and Mashiotta, T. A.: Tropical glacier and ice core evidence of climate change of annual to millennial time sacles, Clim. Change, 59, 137–155, 2003.

Traufetter, F., Oerter, H., Fischer, H., Weller, R., and Miller, H.: Spatio-temporal variability in volcanic sulphate deposition over the past 2 kyr in snow pits and firn cores from Amundsenisen, Dronning Maud Land, Antarctica, J. Glaciol., 50, 137–146, 2004.

Vimeux, F., de Angelis, M., Ginot, G., Magand, O., Casassa, G., Pouyaud, B., Falourd, S., and Johnsen, S.: A promising location in Patagonia for paleoclimate and paleoenvironmental reconstructions revealed by a shallow firn core from Monte San Valentin (Northern Patagonia Icefield, Chile), J. Geophys. Res. Atmos., 113, 1984–2012, 2008.

Wheatley, J. J., Blackwell, P. G., Abram, N. J., McConnell, J. R., Thomas, E. R., and Wolff, E. W.: Automated ice-core layer-counting with strong univariate signals, Clim. Past, 8, 1869–1879, doi:10.5194/cp-8-1869-2012, 2012.

Winstrup, M., Svensson, A. M., Rasmussen, S. O., Winther, O., Steig, E. J., and Axelrod, A. E.: An automated approach for annual layer counting in ice cores, Clim. Past, 8, 1881–1895, doi:10.5194/cp-8-1881-2012, 2012.